Interactive Near-Field Illumination for Photorealistic Augmented Reality with Varying Materials on Mobile Devices

Kai Rohmer, Wolfgang Büschel, Raimund Dachselt, and Thorsten Grosch

Abstract—At present, photorealistic augmentation is not yet possible since the computational power of mobile devices is insufficient. Even streaming solutions from stationary PCs cause a latency that affects user interactions considerably. Therefore, we introduce a differential rendering method that allows for a consistent illumination of the inserted virtual objects on mobile devices, avoiding delays. The computation effort is shared between a stationary PC and the mobile devices to make use of the capacities available on both sides. The method is designed such that only a minimum amount of data has to be transferred asynchronously between the participants. This allows for an interactive illumination of virtual objects with a consistent appearance under both temporally and spatially varying real illumination conditions. To describe the complex near-field illumination in an indoor scenario, HDR video cameras are used to capture the illumination from multiple directions. In this way, sources of illumination can be considered that are not directly visible to the mobile device because of occlusions and the limited field of view. While our method focuses on Lambertian materials, we also provide some initial approaches to approximate non-diffuse virtual objects and thereby allow for a wider field of application at nearly the same cost.

Index Terms—Computer Graphics, Three-Dimensional Graphics and Realism, Augmented and Virtual Realities.

1 Introduction

Mobile devices like smartphones and tablet PCs are part of our everyday life. In combination with the integrated camera, the mobile device can act like a window into an augmented real world [1]. When virtual objects are inserted, their appearance is often inconsistent with the real environment, mainly because of incorrect illumination. So far, a consistent illumination that handles both dynamic scenes and dynamic lighting conditions eluded the mobile platforms. Even though many sophisticated illumination methods allow for plausible global illumination at interactive rates on non-mobile platforms, several applications would benefit from such a mobile system. For instance, applications in interior planning and architecture can be enhanced by convincing in-place visualization of the designer's vision. Bringing back virtual versions of lost or destroyed artifacts would open up new possibilities in the field of cultural heritage. Mobile AR can also be used in movie productions or in the process of creating a theater play by providing previews of the final scene and the created mood to the director at early stages. Furthermore, it is relevant for mobile AR games, as users expect more and more enhanced graphics.

We primarily aim for applications like the augmentation of real prototypes, for which a correct illumination at any place in the scene is required and a perceptively plausible illumination is not sufficient.

To accomplish this, one needs to overcome three problems:

- *Kai Rohmer is part of the Computational Visualistics Group at the University of Magdeburg, Germany. E-mail: kai.rohmer@isg.cs.ovgu.de*
- *Thorsten Grosch is head of the Computational Visualistics Group at the University of Magdeburg, Germany. E-mail: grosch@isg.cs.ovgu.de*
- *Wolfgang Büschel is part of the Interactive Media Lab at the Technische Universität Dresden, Germany. E-mail: bueschel@acm.org*
- *and Raimund Dachselt is head of the Interactive Media Lab at the Technische Universität Dresden, Germany. E-mail: dachselt@acm.org*

- Mobile devices, such as tablets, do not yet have the computational resources necessary for computing interactive global illumination on their own.
- Streaming rendered images from a powerful desktop PC causes a latency that is too high to meet the requirements for seamlessly integrated virtual objects, especially during user interactions and for multiple simultaneous views.
- Real lighting conditions in the dynamic scene need to be captured reliably and limitations caused by occlusions and the limited field of view have to be overcome.

In this paper, we present a novel, *distributed* illumination approach for AR with consistent illumination of virtual objects with direct

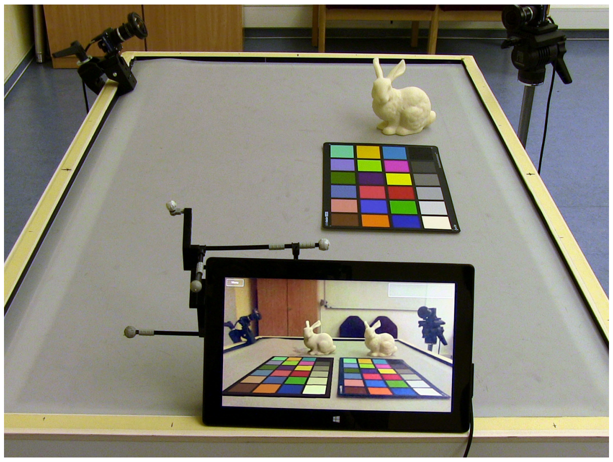

Fig. 1. The tablet camera shows the real world, augmented by virtual objects with consistent illumination, displayed at 27 fps. By using a tracked device, the user can move the tablet freely in the augmented real world and interact with the inserted objects.

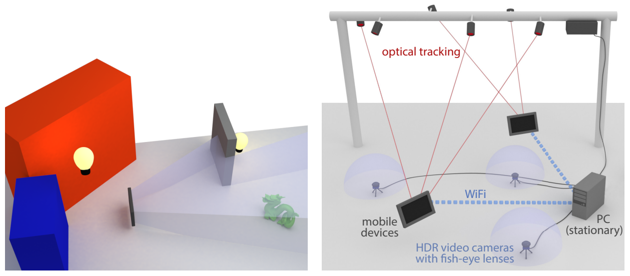

(a) (b)

Fig. 2. (a): The camera image of a mobile device does not see the important light sources required for a consistent illumination of a virtual object. (b): Our hardware setup.

light, indirect light (color bleeding) and shadows of primary and strong secondary lights. Due to the limitations in computational power of the mobile device and the lack of important information (see Figure 2a), we split the illumination into two parts: In the first part, the existing radiance values are captured by a number of HDR video cameras that are placed at different locations in the scene, such that each part of the scene is visible to least one camera. This acquisition process and the extraction of parameters for our lighting model is executed on a stationary PC. Based on the extracted information, we display augmentations with consistent illumination at an interactive frame rate on the mobile device, as shown in Figure 1. To avoid a potential bottleneck of the bandwidth between PC and mobile devices, our illumination model reduces the amount of transferred data that is required for the reconstruction of the environmental lighting condition and the illumination of virtual objects.

Assuming a single mobile device is used to process all tasks from acquisition to rendering, the limitations in computing power and the quality of sensor data might become less important factors in the future. However, due to *occlusions*, it is generally not possible to gather the *dynamic* illumination on all surfaces of the environment from the mobile device position only.

In summary, our main contributions are:

- A new distributed approach for interactive Augmented Reality under dynamic real-world environment lighting,
- A lighting model for correct near-field illumination with compact parametrization to be transferred to one or multiple display devices.

2 Previous Work

AR with Consistent Illumination The first work for AR with consistent illumination was presented by Fournier et al. [2] who invented the differential rendering technique. Further extensions exist for hierarchical radiosity [3] and final gathering [4]. Debevec [5] introduced the high dynamic range (HDR) light probe to capture the distant real illumination. A similar approach was presented by Sato et al. [6] using a fish-eye lens. Grosch [7] introduced differential photon mapping to correctly display reflecting and refracting objects and their changes in illumination. To capture the existing near-field illumination, Corsini et al. [8] used a pair of light probes to estimate the distance of light sources. Using a movable HDR camera with a light probe, Unger et al. [9] captured the complete near-field illumination inside a small region. Even if no information of the surrounding illumination is available, a plausible augmentation can be implemented, as shown by Karsch et al. [10] for legacy photographs. A list of AR illumination techniques can be found in Jacobs and Loscos [11].

Interactive AR with Consistent Illumination For an interactive setting, the first works for AR with consistent illumination were presented by Kanbara and Yokoya [12], and Agusanto et al. [13]. They assume a distant and constant illumination, captured by a light probe. Several approaches simply define the existing illumination manually, e.g., Haller et al. [14] and Pessoa et al. [15]. Gibson and Murta [16] demonstrated how to implement differential rendering on the GPU for distant illumination. This was further extended in [17] for the augmentation of pictures of real rooms, taking near-field illumination into account by combining point lights and an irradiance volume. Grosch [18] showed how this technique can be further improved for the augmentation in a panoramic image viewer. For temporally varying illumination, Havran et al. [19] introduced a sampling approach for an HDR video camera. In Korn et al. [20], two such HDR video cameras were used to estimate the distance of moving light sources. In Grosch et al. [21], a near-field illumination approach was presented for augmentations under daylight in a real room. Similar to our method, an HDR video camera was used to capture the incoming distant radiance, but only from outside the room. We use multiple HDR video cameras inside the room to capture the complex near-field illumination. The idea of differential rendering has been applied to several interactive global illumination methods, including instant radiosity [22], [23], progressive path tracing [24] and light propagation volumes [25]. Kan and Kaufmann [26] presented a partial implementation of differential photon mapping, running at near-interactive frame rates on the GPU. Assuming a single dominant light direction, Nowrouzezahrai et al. [27] introduced a real-time light factorization method that allows soft and hard virtual shadows. Instead of special equipment, an approximate reconstruction of the environmental light is possible from simple objects. This can be a diffuse sphere [28], a special shading probe [29] or only the user's hand [30]. Madsen and Lal [31] demonstrated a photometric reconstruction from shadows, Jachnik et al. [32] used a specular surface. While all these inverse rendering methods only approximate the incoming illumination, we aim for correctly capturing the surface radiance of the whole environment. A first approach to augment live images based on geometry captured by a RGB-D camera was presented by Lensing and Broll [33]. The captured depth image was used here for a fast illumination based only on screen-space information. Meilland et al. [34] reconstructed both 3D geometry and HDR radiance values based on a moving RGB-D camera. For static illumination, a real-time rendering can be performed with correct near-field reflections and shadows of extracted light sources. Gruber et al. [35] demonstrated a probeless approach that displays a visually plausible augmentation. Here, a low-frequency environment map is reconstructed from the illumination of diffuse objects which allows soft shadows between virtual and real objects [36]. Recently, Csongei et al. [37] presented a progressive path tracing solution for AR on a mobile phone based on a pre-recorded environment map. Here, the illumination is simulated on a stationary PC and streamed to the mobile device.

We observe that so far there is no solution for augmented reality with consistent, spatially and temporally varying illumination on a mobile device. The first reason is the low computational power of current mobile devices. Secondly, none of the existing methods addresses an on-line capture process of the spatially and temporally varying near-field illumination. This paper presents a solution to these problems.

3 Overview

Our goal is the consistent illumination of virtual objects on mobile devices in a real environment. Multiple users should be able to interact in the real world with photorealistic augmentations. We thereby focus on an indoor scenario with a difficult, spatially and temporally varying near-field illumination (Figure 2a). This requires the knowledge of the plenoptic function [38], which includes the real radiance values at any point in the scene, viewed from any direction at any time. Based on this information, an interactive global illumination simulation can be computed.

3.1 Hardware Setup and Precomputations

Our hardware setup is shown in Figure 2b: Multiple HDR video cameras are connected to a stationary PC. The cameras are equipped with fish-eye lenses and placed in the scene, such that all regions are visible to least one camera. To enable the measurement of radiance values on real environment surfaces, each camera has to be calibrated in a preprocess. Intrinsic parameters are estimated by using the OCamCalib Toolbox[1] by Davide Scaramuzza and stored in a lookup table to map the captured image on a perfect equidistant projection. To reconstruct the extrinsic parameters, we simply capture a tracked checker board and reconstruct the position of the camera. To acquire absolute real radiance values instead of arbitrary pixel colors, a photometric calibration is necessary. Therefore, we reconstruct the camera response curve using pfstools[2], leading to linear relative radiance values after applying the inverted response curve. By capturing images of an XRite ColorChecker[3] and a least-squares approximation, we obtain a matrix that maps the measured linear radiances onto absolute radiances known for each tile of the checker. A similar process is repeated for each mobile device. Additionally, we estimate another matrix to compensate the color shift introduced by the display. The current position and orientation of the mobile device are captured at runtime. For communication between the stationary PC, mobile devices and the tracking system we use WiFi.

In a preprocess, the geometry and the diffuse materials of the real environment are reconstructed manually using a common DCC tool. The resulting model is a very coarse representation with a simple uv-mapping that is later used as texture atlas (Sec. 3.3).

3.2 Distributed Illumination

Given the HDR information – real radiance at each position of the environment – in combination with the 3D model, we aim for a consistent illumination of virtual objects. Based on measured radiance values of the real environment, there are different choices for interactive global illumination. The obvious solution is to use one of the methods presented in [39] to render the images on a stationary machine and stream the results to all mobile devices. We do not follow this idea for several reasons: First, we need a different image for each mobile device which can lead to a performance break-down on the server side in case of many mobile devices. Additionally, the main difficulty in direct user interaction is the in-time update of the displayed augmented scene. This is because there is a latency in sending notifications of user input to the stationary PC, as well as waiting for the generation, compression, and transmission of the rendered image that is eventually combined with the camera image. We therefore developed an illumination model that distributes the computation between the static PC and the mobile devices.

One option for interactive global illumination is the extraction of a set of virtual point lights (VPLs) [40]. This allows for a complete illumination from all directions with a shadow cast by each VPL. For good quality, at least a few hundred VPLs are required. Unfortunately, only a few VPLs can be computed on a mobile device at interactive frame rates. On the other hand, precomputed radiance transfer (PRT) [41] techniques can be used, which allow real-time illumination with natural light. These techniques work well for low-frequency illumination and diffuse materials. This is especially useful for indirect illumination, such as color bleeding from real to virtual objects. However, high-frequency illumination and hard shadows are difficult to achieve. To solve this problem, we developed a *hybrid* solution that combines the best of both approaches. Our solution is based on the observation that most typical settings consist of a few bright light sources and large low-frequency indirect light regions. We follow the idea introduced in [17] and *split* the incoming light into a *high-frequency* and a *low-frequency* part. There are two reasons for this: First, it allows for an efficient illumination with the desired effects: The high-frequency illumination and shadows can be displayed with a small set of VPLs, while the low-frequency illumination such as color bleeding can be implemented with PRT. The second reason is that this combination *requires only a small amount of data* that needs to be transferred between the stationary PC and the mobile devices, enabling interactive update rates. In contrast to that, Gibson et al. [17] create a subdivision of the environment geometry and treat the resulting patches as source and/or receiver. Based on occlusions between source and receiver patches because of virtual objects, the influence on the background is computed in the sense of differential rendering. Since we do not work with patches and links between them, we only make use of the fundamental idea to classify the regions with the highest intensity as primary light source.

3.3 Pipeline Overview

The whole pipeline, from capturing images of the real world to displaying the augmented image using the distributed illumination, is summarized in Figure 3: The HDR video cameras with fish-eye lenses capture the existing radiance values. Then, on the stationary PC each image is projected onto the reconstructed 3D geometry using a hemispherical projection and shadow mapping. The recorded radiance values are stored in a *radiance atlas* which describes a 1:1 mapping of 3D scene points to atlas texels (Sec. 4.1). To capture the illumination at all relevant parts of the environment, we use multiple cameras. Therefore, areas seen by more than one camera receive multiple measurements leading to a more robust result. For an illumination at both interactive speed and high quality on a mobile device, we proceed as follows: The radiance atlas is split into two parts: A *direct* (high-frequency) radiance atlas and an *indirect* (low-frequency) radiance atlas (Sec. 4.2). The direct radiance atlas is transformed into a small set of area lights (Sec. 4.3), which is transferred to

1. https://sites.google.com/site/scarabotix/ocamcalib-toolbox
2. http://resources.mpi-inf.mpg.de/hdr/calibration/pfs.html
3. http://xritephoto.com/ph_product_overview.aspx?id=1192

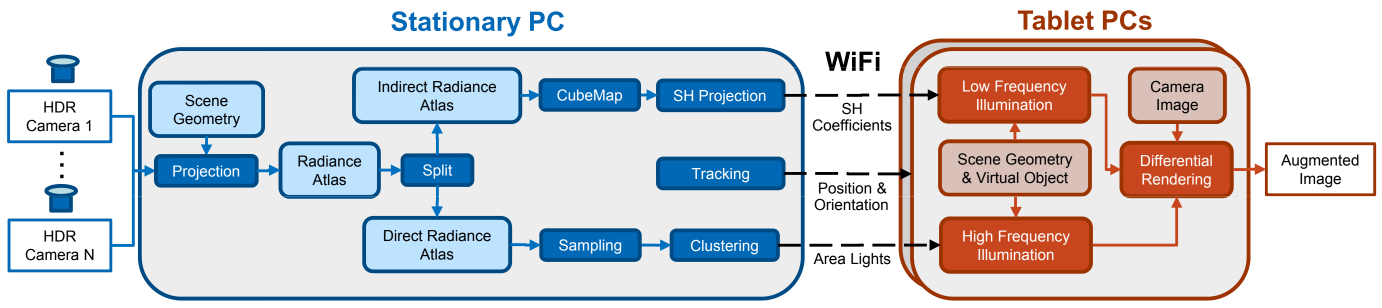

Fig. 3. The whole pipeline for distributed illumination from capturing multiple images of the real environment to the augmentation of the live camera stream on mobile devices.

the mobile device. PRT is used for low-frequency illumination on the clients. Thus, the indirect radiance is transformed into the spherical harmonic (SH) basis (Sec. 4.4) and the resulting coefficients are transferred to the tablet PC as well. Based on this information, the illumination of virtual objects can be computed quickly on the tablet PC without streaming any images. Using differential rendering, the virtual object can then be inserted into the tablet camera image with correct appearance and shadows (Sec. 5).

4 Server Computations

We explain the server computations of our method based on a simple synthetic example shown in Figure 4a.

4.1 Acquiring the Radiance Atlas

We use a texture atlas to record radiance values for all points in the scene. To update the current lighting conditions, each HDR camera permanently projects its radiance values into the atlas. This is implemented by rendering the reconstructed scene with a vertex shader that replaces the vertex position with its texture coordinate and outputs the world position along with the vertex normal to the pixel shader stage. There, we project the world position of each fragment into the camera image space to get the corresponding image coordinate. Subsequently, we sample the camera image and a previously generated artificial depth image at this location to decide the visibility of the currently processed texel in a way similar to shadow mapping (see Figure 5). Since triangles that are not facing the camera cannot be seen, they are rejected during the rendering into the atlas, depending on the dot product of normal and view direction. When multiple cameras see the same region, we compute a weighted average of the camera images (see Figure 4b).

To account for the low resolution in the border regions of a fish-eye projection, we use the angle α_i to the main camera direction $\mathbf{d}_i$ as a weighting. We also use the angle β_i between the view direction and the surface normal $\mathbf{n}$ to compensate inaccuracies during the reconstruction by considering steep angles less reliable. As final weight for a texel of camera i we are using $w_i = \cos\alpha_i \cos\beta_i$. Here and in the following the cosine is clamped to the interval $[0,1]$ to avoid special treatment of negative values.

Since each texel in the atlas can become an indirect light source, we store both position and normal to correctly place and rotate the light. For photometric correctness, each texel stores both the radiance value and the spatially varying world-space area of the texel. To compensate artifacts at texture seams, we apply a dilation over the 8 neighbors with a range of 2 texels.

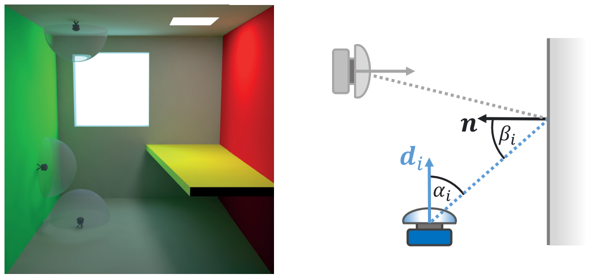

(a) (b)

Fig. 4. Acquiring the radiance of a simple synthetic scene with three HDR cameras (a) and the angular weighting used for merging the projected camera images (b).

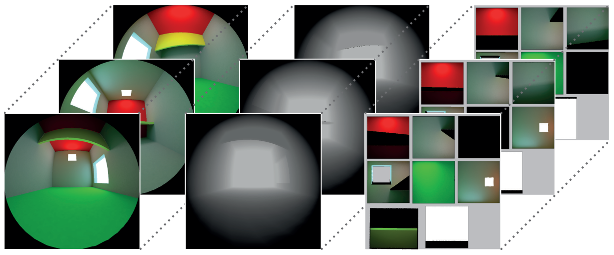

(a) Camera Images (b) Virtual Depth Renderings (c) Projection into the Atlas

Fig. 5. Acquiring the radiance atlas for the synthetic scene with three HDR cameras. Each HDR camera records a fish-eye image of the scene. Additionally, a depth buffer is rendered for each camera using the reconstructed scene. Using the depth buffer for visibility tests, the camera image is then projected into the radiance atlas (right). Note that each camera has only a partial information of the total scene radiance.

4.2 Splitting the Radiance Atlas

To determine the radiance L at any point $\mathbf{x}$, seen from direction ω, we integrate over the hemisphere Ω to solve the rendering equation [42]

$$L(\mathbf{x},\omega) = \int_{\Omega} f_r(\mathbf{x},\omega_i,\omega)\, L_{in}(\mathbf{x},\omega_i)\, \cos\theta_i \, d\omega_i \ , \quad (1)$$

where L_{in} is the incoming radiance from direction ω_i, f_r is the bidirectional reflectance distribution function (BRDF), and θ_i is the angle between ω_i and the surface normal at $\mathbf{x}$. For efficiency reasons, we separate the reflected radiance in direct radiance L_{Dir} and indirect radiance L_{Ind}

$$L(\mathbf{x},\omega) = L_{Dir}(\mathbf{x},\omega) + L_{Ind}(\mathbf{x},\omega) \ , \quad (2)$$

where L_{Dir} corresponds to the direct radiance caused by light sources and strong indirect lights and L_{Ind} is the remaining indirect

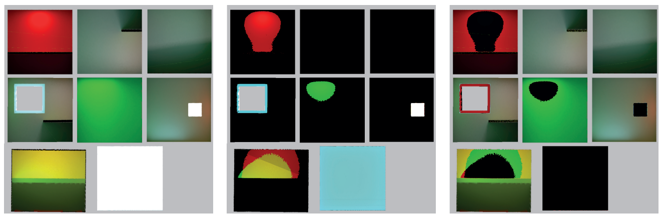

Fig. 6. The radiance atlas (a) is split in direct radiance - here stored as intensity (b) and indirect radiance (c). Note that the direct radiance atlas contains both the light sources and bright indirect regions. The separation is computed per color channel to allow sources in monochrome regions that would have a low gray scale brightness.

radiance. This means that we decide for each direction of the hemisphere around $\mathbf{x}$ whether it corresponds to incoming direct radiance Ω_{Dir} or incoming indirect radiance Ω_{Ind}:

$$\begin{aligned} L_{Dir}(\mathbf{x},\omega) &= \int_{\Omega_{Dir}} f_r(\mathbf{x},\omega_i,\omega)\, L_{in}(\mathbf{x},\omega_i)\, \cos\theta_i \, d\omega_i \\ L_{Ind}(\mathbf{x},\omega) &= \int_{\Omega_{Ind}} f_r(\mathbf{x},\omega_i,\omega)\, L_{in}(\mathbf{x},\omega_i)\, \cos\theta_i \, d\omega_i \ . \end{aligned} \tag{3}$$

To implement this separation, we split the radiance atlas in a *direct radiance atlas* and an *indirect radiance atlas*. For this, we determine a *threshold value*: Texels in the atlas with a radiance larger than the threshold are assigned to the direct radiance atlas, the other texels are assigned to the indirect radiance atlas. To allow for varying lighting conditions, this threshold is adjusted *dynamically*. For this purpose, we provide a user-defined parameter τ that describes how much of the *total* amount of light in the scene should be assigned to the direct light. To determine the threshold radiance based on τ, we first compute the histogram of *all* radiant intensity values in the atlas. We then accumulate the radiant intensity values from high to low until the given percentage is reached. In this way, the direct radiance atlas always contains a certain amount of direct light or strong indirect light. Figure 6 shows an example for this separation. The selection of a suitable value for τ is discussed in Sec. 6.7.

4.3 Finding Direct Light Sources

After splitting the atlas, the direct radiance at $\mathbf{x}$ is computed by summing up all N_{Dir} texels in the direct radiance atlas:

$$L_{Dir}(\mathbf{x},\omega) \approx \sum_{i=1}^{N_{Dir}} f_r(\mathbf{x},\omega_i,\omega)\, L_i\, V(\mathbf{x},\omega_i)\, \cos\theta_i \, \frac{\Delta A_i \, \cos\theta}{r^2} \ , \tag{4}$$

where L_i and ΔA_i are the radiance and area of texel i, and V is the binary visibility function. The distance between sender and receiver is r and the angle to the sender normal is θ. To simplify the computation, we now group the N_{Dir} texels from the direct radiance atlas into a *low* number of $j = 1..M$ clusters. In accordance with [43] we denote the clusters as *virtual area lights* (VALs). The unoccluded direct radiance at $\mathbf{x}$ due to a VAL j is then given by:

$$L_{VAL_j}(\mathbf{x},\omega) = f_r(\mathbf{x},\omega_j,\omega)\, \frac{I_j \cos\theta_j \, \cos\theta}{r^2} \ , \tag{5}$$

where the radiant intensity I_j of VAL j is computed by summing up all N_j texels assigned to this cluster:

$$I_j = \sum_{k=1}^{N_j} L_k \, \Delta A_k \ . \tag{6}$$

Therefore, the direct radiance can be approximated by summing up all M VALs:

$$L_{Dir}(\mathbf{x},\omega) \approx \sum_{j=1}^{M} L_{VAL_j}(\mathbf{x},\omega)\, V(\mathbf{x},\omega_j) \ . \tag{7}$$

Note that for $M = N_{Dir}$, this yields Eq. (4) without $V(\mathbf{x},\omega_i)$.

To avoid flickering, these extracted virtual area lights have to be coherent under temporally varying illumination. To accomplish this, we modified the clustering method described by Dong et al. [43]. Instead of generating VPLs by sampling a reflective shadow map using a Halton sequence, we draw a set of samples in the direct radiance atlas by importance sampling on the GPU. By dividing the radiance of each pixel by the overall radiance of the direct radiance atlas we can define a probability density function. Prefix sum scans are then used to generate cumulative density functions (CDF) which are sampled using the inverse CDF method for 2D. Similar to Dong et al., we use k-means clustering with positions and normals as weight to generate clusters of the samples. In Sec. 5 we estimate the visibility function for each VAL by a single shadow map which also follows Dong et al. [43]. To correctly compute the radiant intensity I_j of each VAL using Eq. (6), each texel in the direct radiance atlas is assigned to its closest cluster center, using the same distance metric. Finally, the data to be transferred to the mobile device for each VAL is the following: Position (12 bytes), normal (4 bytes, compressed), radiant intensity (12 bytes) and area (4 bytes). In total, these are only 32 bytes per VAL. The total number of VALs is a time-quality tradeoff, in our experiments we use $8 \leq M \leq 64$.

Note that we only use the direct radiance atlas for the VAL extraction and ignore the current position of the virtual objects. As an alternative, an environment map could be rendered from the virtual object center position. The drawback of this option is that we might miss some important light sources which are not visible from the center of the virtual object. Additionally, the global VAL selection achieves a better temporal coherence, and in the case of multiple virtual objects, only one set of VALs is used which follows the concept of a consistent global light model.

4.4 Compressing Indirect Light

For the indirect light L_{Ind}, we assume that the remaining illumination in the indirect radiance atlas is of low frequency. In this case, a compression using spherical harmonics (SH) can be applied to the environment light around the virtual object. For a diffuse virtual object with reflection coefficient ρ, it is sufficient to use only the first $K = 9$ basis functions for an illumination with a barely visible error, as shown in [41], [44]. Given a vertex v at position $\mathbf{x}$, the indirect radiance is computed as a simple dot product:

$$L_{Ind}(\mathbf{x},\omega) \approx \frac{\rho}{\pi} \sum_{k=0}^{K-1} C_k C_{vk} \ , \tag{8}$$

where the coefficients C_k and C_{vk} are obtained by a projection onto the SH basis function Y_k:

$$C_k = \int_{\Omega_{Ind}} L_{in}(\mathbf{x},\omega_i)\, Y_k(\omega_i)\, d\omega_i \tag{9}$$

$$C_{vk} = \int_{\Omega} V(\mathbf{x},\omega_i)\, \cos\theta_i \, Y_k(\omega_i)\, d\omega_i \ . \tag{10}$$

The C_k coefficients can be interpreted as the amount of light that is incident from *all* directions of the surrounding. Corresponding

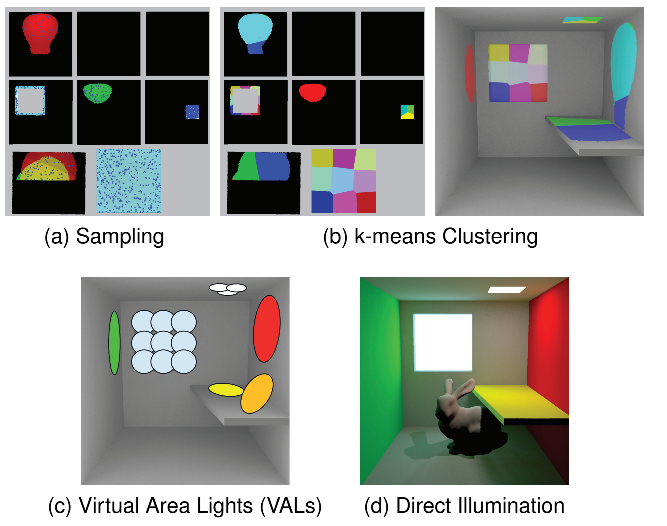

Fig. 7. VAL extraction for direct light: Importance Sampling on the direct radiance atlas (a). Using k-means clustering, these samples are grouped in M clusters (b). Each texel is assigned to the closest cluster center. Integration over each cluster leads to M VALs (c) that are used for direct illumination of a virtual object (d).

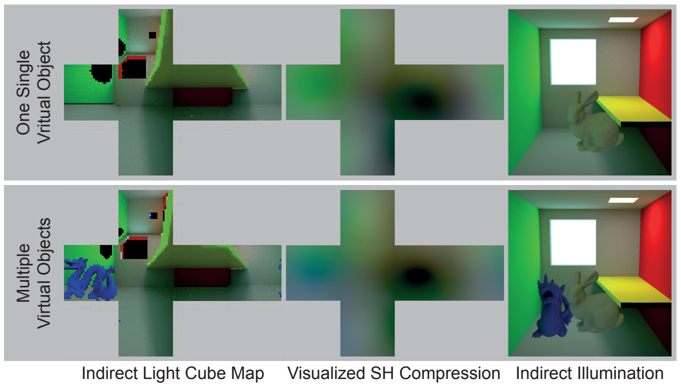

Fig. 8. To estimate the indirect illumination of a virtual object, we first render a cube map with the indirect radiances from the object center (left). This is projected into the first nine SH basis functions (center) which allows a real-time illumination of a virtual object (right). The second row shows multiple virtual objects with mutual interreflections, like the blue color bleeding from DRAGON to BUNNY.

to that, the C_{vk} coefficients at a vertex v describe a set of directions from which incident light is *not occluded*. As the SH basis functions are orthonormal, the dot product of both is then the amount of *incident unoccluded* light from all directions at the vertex. The coefficients C_{vk} of the transfer function $V\cos\theta_i$ are *static*, so they can be precomputed and stored per vertex at the virtual object. In contrast, the coefficients C_k of the environment map L_{in} *change* whenever the incoming illumination changes. We therefore render a low-resolution $(6\times 32\times 32)$ cube map from the virtual object's position with the indirect radiance atlas as texture of the surrounding scene. Then, this is projected to the first nine spherical harmonic basis functions Y_k and the resulting coefficients C_k are transferred to the mobile device. Using RGB float values, these are only $9\times 3\times 4 = 108$ bytes in total. In case of multiple mobile devices, the same coefficients can be reused. In case of multiple virtual objects, this process is repeated for each object. The computation cost for this step is small (see Sec. 6).

In fact, we are able to also consider the indirect light transmission between virtual objects with a small overhead by including the other virtual objects during the indirect light estimation of the one that is updated. This is shown in Figure 8 (bottom) for the BUNNY interacting with a blue DRAGON. To keep the additional effort low, the objects are illuminated by PRT, too. Therefore, we render another cube map containing direct and indirect light to derive SH-coefficients with the correct amount of light. In summary, we are rendering $2n$ cube maps, each containing $n-1$ virtual objects and the reconstructed scene in order to achieve additional indirect light transmission between n virtual objects. Note that these interreflections cover $b-1$ bounces for objects that are static for b iterations.

To meet the real-time requirements we need to be able to perform this compression for multiple cube maps in a narrow time frame. Therefore, we precompute SH-coefficient weights C_{wtk} for each cube map texel ω_t and use the GPU to weight and accumulate the radiance $L(\omega_t)$ per texel:

$$C_{wtk} = Y_k(\omega_t)\,\omega_t \tag{11}$$

$$C_k \approx \sum_{t=1}^{6\times 32\times 32} L(\omega_t)\,C_{wtk}\ . \tag{12}$$

Note that Eq. (11) and Eq. (12) represent a discretization of Eq. (9) that can be mapped to a scan program on the GPU. The same compute program can be used to estimate C_{vk} (see Eq. (10)). Here, we render a cube map at each vertex v. To estimate the visibility V, the object is colored black and rendered into a white cube map. Additionally, we account for $\cos\theta_t$ by using the angle θ_t between the vertex normal and the direction of ω_t leading to Eq. (13). Note that the cosine is clamped to the interval $[0,1]$ to integrate the visible hemisphere only.

$$C_{vk} \approx \sum_{t=1}^{6\times 32\times 32} V(\omega_t)\,\cos\theta_t\,C_{wtk} \tag{13}$$

5 RENDERING ON THE CLIENT

Due to the described separation of illumination, the final image generation on the client only requires lightweight operations for a mobile device with limited rendering capabilities: For each VAL, we compute the direct radiance and visibility using shadow mapping Eq. (7). This is added to the indirect illumination which is computed per vertex by applying Eq. (8) using the stored coefficients C_{vk} and the transferred coefficients C_k. To display virtual shadows with correct brightness, we use differential rendering and subtract direct radiance in the virtual shadows.

To improve the rendering performance, we use a *tile-based deferred shading* based on Andersson [45]. Compared to simple forward rendering and non-tiled deferred rendering, a tile-based approach reduces overdraws to a minimum because each final screen texel is processed only once. Additionally, the G-Buffer (see Figure 9) needs to be read only once, which improves performance since memory accesses are expensive.

In the first pass, the reconstructed and the virtual scene are rendered into one G-Buffer containing projection space depth, world space normal, diffuse reflection coefficients, and indirect radiance as well as flags to distinguish virtual from real objects (see Figure 9). To avoid unnecessary geometry processing, we

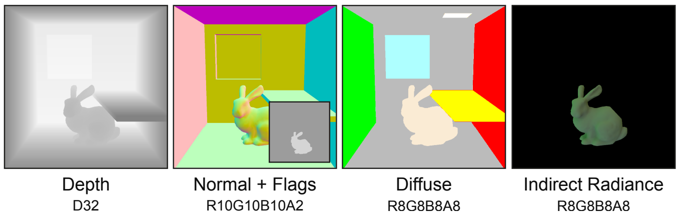

Fig. 9. G-Buffer: an off-screen buffer containing geometry and material information of the reconstructed and virtual scene per pixel.

calculate the indirect radiance for virtual objects by PRT in the vertex shader. Hence, we need to render the scene only once, except for the shadow map generation described later in this section.

The second pass handles light calculations and the composition of the augmented image in one single compute shader program. Thus, the screen is divided into tiles of 8×8 texels – which performed best in our tests – that are processed by a thread group of 64 threads per tile. Each thread then executes the following steps:

1) Read the background image and G-Buffer data for the corresponding texel and construct the view frustum around the tile. Near and far plane are determined by the minimum and maximum occurring depth value within the tile.
2) Cull the VAL assigned to the thread if the view frustum is entirely in the negative hemisphere of the VAL. Due to the Lambertian emission of the VALs, such a VAL does not contribute to the illumination of the tile. Because of the group size, 64 VALs can be treated simultaneously. If there are more VALs than threads per tile, this process is performed in a loop. Lights not culled are added to a shared list, containing $m \leq M$ visible VALs.
3) Perform visibility and shading operations to illuminate the surface position $\mathbf{x}$ at the texel by all remaining m VALs in the group shared VAL list. For differential rendering, we accumulate the radiance L_{VAL_j} of all VALs depending on the texels' flags. For texels marked virtual we store radiance that is not shadowed, neither by real nor by virtual objects. For non-virtual texels, we store radiance that is shadowed by virtual but not by real objects. In essence, we estimate the light that should be missing because of new virtual shadows.
4) Combine the results of step 3, the background color, and the indirect radiance using Eq. (14) for texels marked and not marked as virtual. The visibility at $\mathbf{x}$ from $VAL\ j$ in the reconstructed scene is referred to as V_j, where $\hat{V}_j$ is the visibility in the virtual scene.

$$L = \begin{cases} L_{Ind} + \sum_{j=1}^{m} V_j \cdot \hat{V}_j \cdot L_{VAL_j} & \text{if virtual} \\ L_{background} - \sum_{j=1}^{m} V_j \cdot (1 - \hat{V}_j) \cdot L_{VAL_j} & \text{otherwise} . \end{cases} \tag{14}$$

As described earlier, we use two shadow maps per VAL to cover shadows from reconstructed and virtual objects [16], [23]. This is necessary to prevent virtual objects from casting shadows through real objects (see Figure 10b). Using only one shadow map containing the closest distance in light space can lead to correct shadows (green). But without the distance of the closest reconstructed object we are not able to identify the correct shadow receiver and add wrong shadows (red) on every further surface. Hence, we need $2M$ shadow maps for direct illumination with M VALs, which is not feasible for large M in real-time. To reduce the geometry processing overhead we update 16 shadow maps at once by using a geometry shader for duplicating the primitives and rendering to multiple viewports simultaneously. Therefore, we organize our shadow buffer in a texture array containing 4×4 shadow maps per slice (see Figure 10a). To adjust to the narrow time budget, we update only one slice of the virtual shadow buffer and one slice of the reconstructed shadows per frame. The update order follows round robin, but currently updated VALs are preferred. To obtain good shadows with low resolution we construct each shadow frustum to closely fit all visible virtual objects and use this frustum for both virtual and reconstructed shadows maps. The reconstructed geometry between light and near plane is projected onto the near plane.

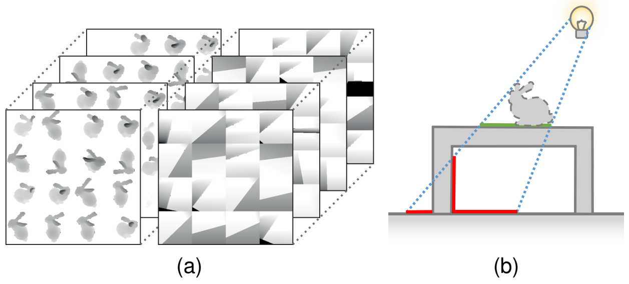

Fig. 10. Two shadow maps per VAL (a) are required to avoid double shadowing from virtual objects (dashed contour) in regions that are shadowed in the real environment (b).

6 Results

In this section, we will report the results that are obtained by our distributed approach for augmenting live camera streams with virtual objects illuminated by the dynamically captured real world environment. All performance experiments for rendering were run on a Microsoft Surface Pro with Intel i5-3317U CPU, 1.7 GHz, 4 GB RAM and Intel HD Graphics 4000. The stationary PC used for image acquisition and calculation of the light model parameters was equipped with an AMD Phenom II X4 965 CPU, 3.4 GHz, 8 GB RAM and an NVIDIA GeForce 580 GTX.

For comparison in quality and performance we decided to evaluate the synthetic Cornell Scene used in Sec. 4 to avoid inaccuracies caused by the camera sensors and lenses as well as during the reconstruction process. Nevertheless, results of real world scenarios are demonstrated in the later part of this section. The scene was designed to be as simple as possible while showing the most important interactions between real and virtual objects. In particular, there are shadows from virtual on real objects and vice versa, virtual objects occluding real objects and vice versa, and there is a strong indirect light that causes color bleeding. The radiance of the small light at the ceiling is 15 $^{W}/_{srm^2}$ and thereby 5 times brighter than the window with 3 $^{W}/_{srm^2}$. The scene is augmented by a Bunny with 2.5k triangles and the resolution of the G-Buffer is 960×540, where not otherwise stated.

6.1 Comparison

To evaluate our approach we compare it with a standard VPL-based lighting, PRT and different combinations of light clustering and splitting into direct and indirect light. To achieve fair results, we used the same renderer with all optimizations by tiled rendering and simplifications during shadow map updates for rendering VPLs as we do in our case. For PRT we were also using the G-Buffer to treat occlusions between real and virtual objects as well as the same calculation of indirect light used in our approach, but we disabled all direct light calculations and shadow map updates since they cannot be used with PRT. Figure 11 shows results of the different methods depending on the number of direct light sources. For the synthetic scene we created a path traced reference image, depicted in the lower right corner. Above this ground truth solution the result of simple PRT without any directional lights is shown. In the first row, the classic Monte Carlo-based VPL lighting is depicted. To generate VPLs, the radiance atlas was sampled using the gray scale intensity as density function p. While the position is directly read from the atlas at sample position s, the radiant intensity of the resulting VPL is calculated by:

$$I_{VPL} = \frac{1}{N_{VPL}} \cdot \frac{I_s}{p_s} , \qquad (15)$$

where N_{VPL} is the number of VPLs (assuming a diffuse surface).

The second row combines the classic VPL lighting with our light separation. Instead of sampling the complete radiance atlas, we just sample the direct light atlas (see Figure 7a). The indirect light is compressed to spherical harmonics as we do in our approach. The third row shows clustered VPLs without light separation. In this case, we apply our direct light clustering step to the classical VPL method. Here we draw 4k samples, cluster them by k-Means and integrate the radiance atlas to result in one VPL for each cluster, as described in Sec. 4.3. The last row contains the final results of our approach with light separation and clustering.

6.2 Evaluation

In comparison with the ground truth image, the result of the PRT method shows significant differences. Besides the lack of shadows, there is a visible shift in the color of shading. The environment coefficients used for this image were derived from a cube map rendered at the object center from where the bright red wall is only slightly visible. This explains the cold tone of the image and why PRT alone is not a good choice for near-field illumination, even though the measured timings are best.

Evaluating the classical VPL approach confirms the expected behavior known from instant radiosity implementations [22], [23], [40]. A large number of lights is required to converge against the correct solution. We stopped at 512 sources, which produced a result close to the reference image in 503 ms.

By separating high-frequency from low-frequency light the regions to sample for VPL generation become smaller. In combination with PRT-based low-frequency illumination, the visual quality of the results increases, especially for a low number of light sources. Because of the smaller sample regions, the point lights concentrate in bright areas, which leads to more plausible shadows as second benefit. The additional computation cost for PRT lighting is constant and rather low compared to the direct lighting. Note that these two methods without light clustering are not coherent over time for smaller light counts. This results in a distracting flickering and is not suitable in most scenarios. To provide an impression, we refer to the accompanying video.

The experiments with clustered VPLs showed an improved spatial coherence but did not lead to a temporal coherent illumination because of the large cluster sizes that need to cover the whole radiance atlas. For the client, there is no difference to classical VPLs in terms of calculations for lighting, which was confirmed by equal timings.

The results of our approach, depicted in the last row, contain features of both improvements. The separation of the radiance atlas leads to smaller areas to be sampled, hence the light sources concentrate in the brightest regions. The additional clustering leads to coherent light positions and thus coherent virtual shadows. It also allows to integrate the area per light and to approximated the shape by a disc. Hence, virtual objects close to light sources do not show the singularities of classic point lights. Considering the measured timings, there is no difference compared with the approach in row two, since there is no difference in rendering on the client side. Comparing the images created with varying numbers of VALs reveals only slight differences in the shading of the virtual object. The most obvious distinction can be found in the quality of the shadows, especially at the transition from the virtual to the real shadow cast by the yellow board. A drawback of our approach can be observed in the shadowed region of the BUNNY which is too bright in comparison with the reference image. One reason for that is the limited number of SH coefficients C_k and the lack of details in the reconstructed indirect light. Another influencing factor is that the cube map is only valid for the center of the virtual object. Other locations on the virtual object, e.g., below the yellow board, have a slightly different environment illumination. This problem could be addressed by evaluating the indirect light at multiple locations and interpolating the SH coefficients per vertex during rendering which leads to an approach similar to irradiance volumes [46]. Finally, there is another aspect that contributes to a too bright indirect lighting. The indirect radiance estimation at the center of the virtual object by cube map rasterization does not consider the shadows cast by any virtual objects.

6.3 Light Extraction Performance

All tasks executed by the server are implemented on the GPU. Since the results are transmitted asynchronously, the computations do not affect the rendering performance discussed in the next paragraph. However, an interactive update rate improves the visual quality of the rendering while moving virtual objects and reduces the time that is needed to respond to changes in the dynamic environment. Table 1 contains the timings measured with our current implementation. The individual steps are not executed in the listed order. The first block is only required if the tracking system reported a moving real object. The operations on the camera images in the second block are applied only if a camera captured a new image during the last iteration. The latter is influenced by the type and number of cameras used, their resolution, and the available bandwidth for the transfer to the GPU.

The time to update the indirect light coefficients depends on the number of virtual objects. Figure 12 illustrates the increasing effort with growing number of virtual objects. As described in Sec. 4.4, we include the other virtual objects to take account of indirect transmission between the objects. Hence, the time required for rendering a cube map increases with the number of objects while the duration for compressing the cube maps into SH-coefficients is constant. Note that the time to update the indirect

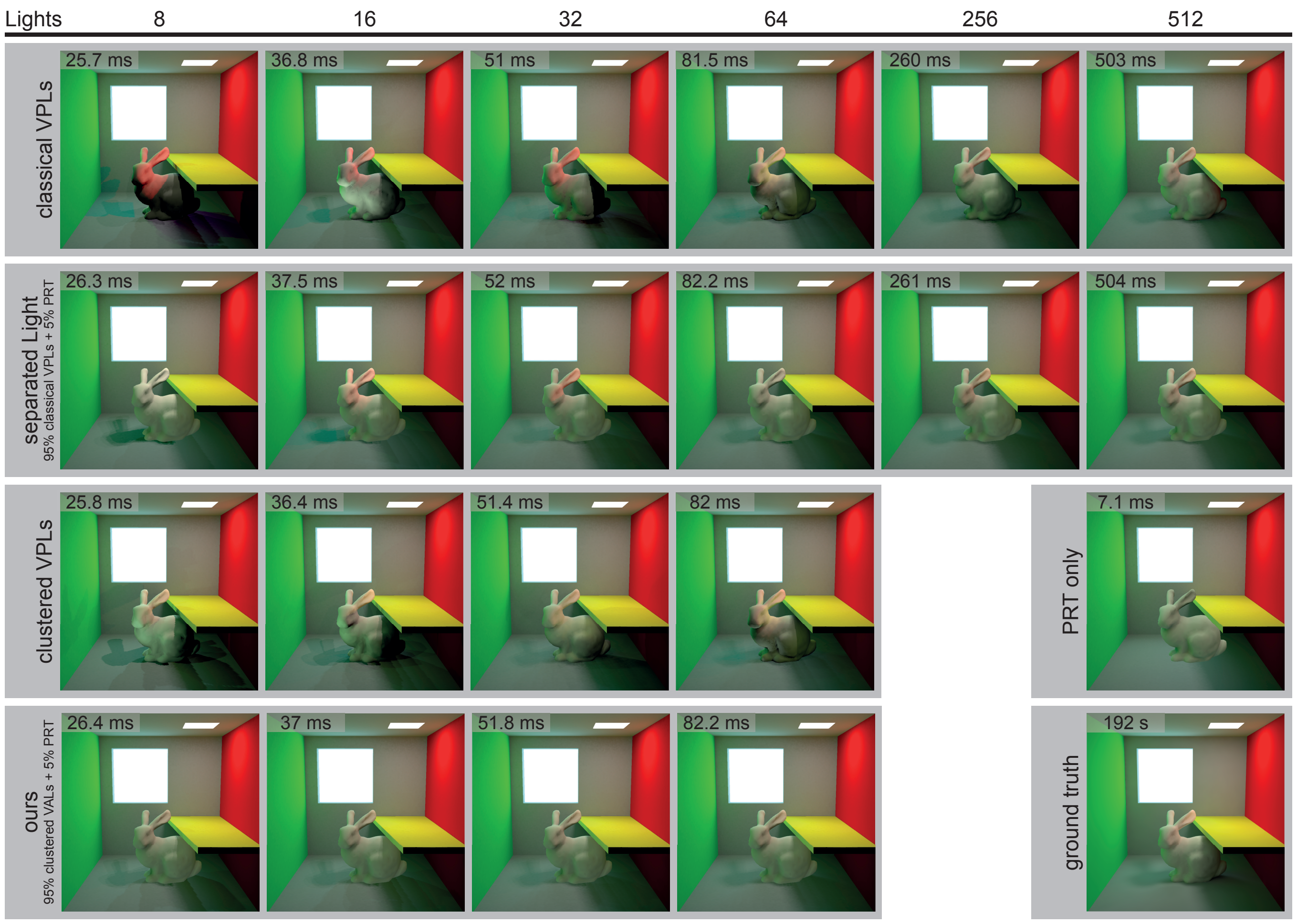

Fig. 11. Comparison with classical VPL lighting, PRT and combinations

TABLE 1
Timing breakdown in ms for the stationary PC at an atlas resolution of 1024×1024, 4 HDR cameras, 4k direct light samples and 16 clusters with 20 iterations per clustering step.

Update Atlas (for dynamic scenes)	
Position, normals and area	0.5 ms
Dilatation	1.33 ms
Acquiring the Radiance Atlas (* per camera)	
Acquire color image *	2.35 ms
Render depth image *	0.26 ms
Project into atlas *	0.44 ms
Combine radiance atlas	0.58 ms
Splitting the Radiance Atlas	
Find separating threshold	9.1 ms
Split into direct and indirect atlas	0.53 ms
Finding Direct Light Sources	
Sampling (4k Samples)	6.67 ms
k-Means clustering (M=16)	7.3 ms
Integrating cluster radiances	17.5 ms

light without interaction between virtual objects would be equal to the duration measured for one virtual object. The rendering of an extra cube map with direct and indirect light is not necessary in this case.

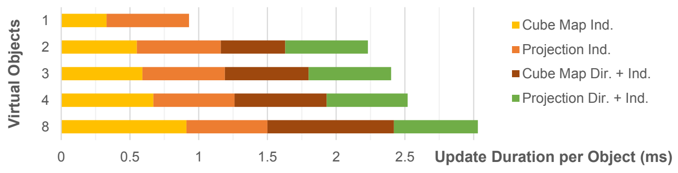

Fig. 12. Timings for updating the indirect light coefficients per object. Measured in the CORNELL SCENE with multiple virtual BUNNIES.

6.4 Rendering Performance

As noted in Sec. 5, the tile-based approach reduces the number of geometry processing passes, overdraw, and G-Buffer accesses per texel. Nevertheless, the G-Buffer resolution is the most dominant factor on the rendering performance. Figure 13 illustrates the increasing time per frame with growing light count and resolution. In consequence of the tiled rendering the timings grow almost linearly with the number of rendered tiles.

In Figure 14 the frame timings are broken down to five steps. The acquisition of the background image, the rendering of reconstructed shadows, and the generation of the G-Buffer are independent of the number of VALs. The update of 16 virtual shadow maps takes 2.2 ms if 16 or more lights are present. The largest part of the time is spent on calculating the direct illumination and visibility. After a constant offset, the required time increases linearly with the number of lights.

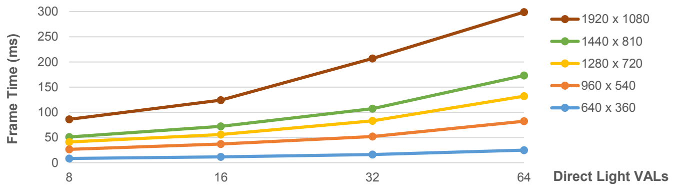

Fig. 13. Influence of the G-Buffer resolution on the frame time. Timings measured for augmenting the CORNELL SCENE with the virtual BUNNY.

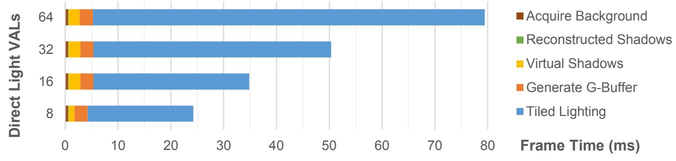

Fig. 14. Timings with respect to the number of VALs measured for augmenting the CORNELL SCENE with the virtual BUNNY broken down and accumulated.

Because of the deferred rendering, the impact of geometry complexity on performance is assumed to be low as each model has to be rendered only once to generate the G-Buffer. The result of the evaluation with virtual models of different complexity is depicted in Figure 15. As anticipated, the time required to create the G-Buffer increases with the number of primitives, up to 10 ms for 260k triangles. The other step that needs to render the virtual geometry is the update of the virtual shadows. Since we are processing 16 shadow maps per iteration, the duration grows exponentially up to 216 ms for the largest model. Fortunately, this large number is not relevant in practice, since low-poly models can be used for rendering shadow maps of low resolution. Hence, a few hundred primitives are sufficient for the 128×128 shadow maps we used in our examples, and highly detailed models are only required during the G-Buffer generation.

6.5 Real World Scenarios

To measure the real-world radiance values, we use Matrix Vision mvBlueFOX-IGC200 HDR video cameras with 180 degrees fish-eye lenses. For tracking, we use OptiTrack with 12 infrared cameras, capturing a range of approximately 3×2 meters.

Figure 16 contains an overview of an acquired real scene. The first row shows the input of three different cameras. To illustrate the corresponding reconstructed scene, we rendered the wire-frame model as overlay. The second row shows the projections of the camera images into the atlas where flaws in the reconstruction and the registration of the cameras become visible. The merged atlas (left), the direct light atlas (center) and the indirect light atlas (right) are depicted in the last row. Note that some ghosting artifacts caused by the mentioned inaccuracies become visible,

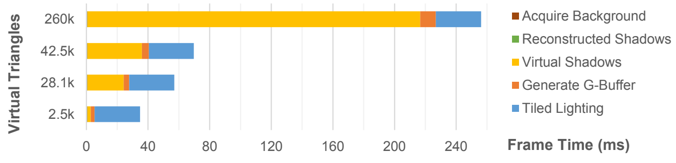

Fig. 15. Timings with respect to vertex count measured for augmenting the CORNELL SCENE with different virtual models and 16 lights broken down and accumulated.

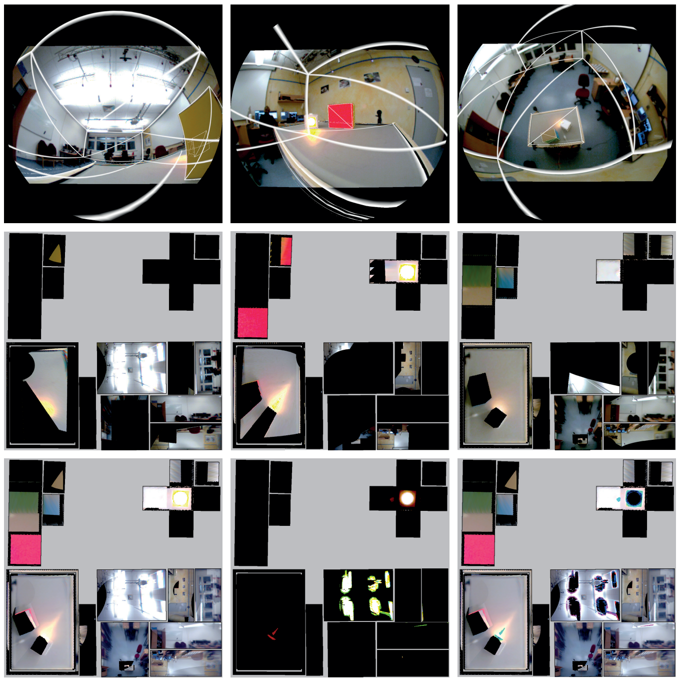

Fig. 16. Real scene acquired by three cameras (first row). Images projected into the atlas (second row). Merged, direct and indirect atlas (last row from left to right).

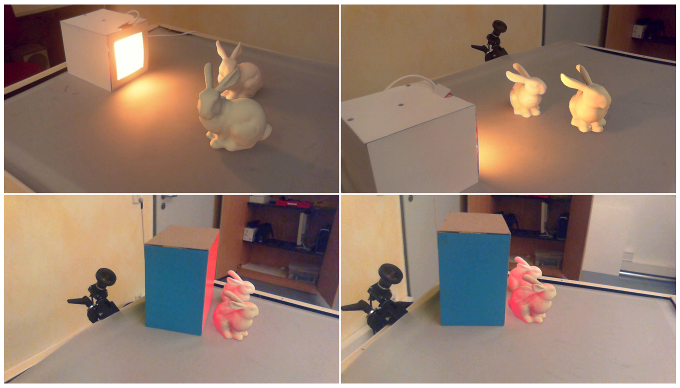

Fig. 17. A virtual BUNNY in front of its real counterpart, illuminated by a local light source (top) and a strong indirect light (bottom). In both cases, the sender becomes invisible after user movement.

but their influence on the final result is low as long as the receiver material is diffuse and the overall radiance matches the real light conditions.

Figure 1 shows the consistent appearance of a 3D-printed and a virtual BUNNY side-by-side. We added a real and a virtual color checker to show the quality of the reproduced colors. To verify the correct capture process of the *near-field* illumination, we place the BUNNY close to a local light source and a strong indirect light, as shown in Figure 17. An interactive session from the accompanying video is shown in Figure 18, demonstrating both temporally and spatially varying illumination. The performance in real and synthetic scenes has been very similar in all our experiments. This is because the cost for transferring the mobile camera image to VRAM and the cost for rendering the synthetic background image compensate each other.

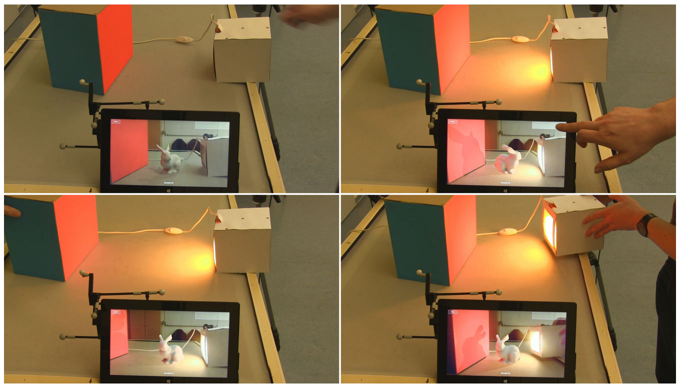

Fig. 18. Moving tracked objects: Initial configuration (top left), user switches on the light and rotates the BUNNY at 27 fps (top right), red color bleeding disappears when the box is moved away (bottom left) and direct light changes after light movement (bottom right).

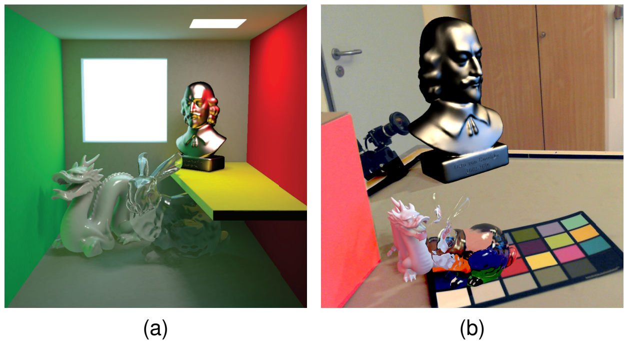

Fig. 19. A synthetic (a) and a real scene (b) augmented by objects with non-diffuse BRDFs. Both images show a glossy DRAGON, a glass BUNNY and a metallic OTTO bust.

6.6 Non-diffuse BRDFs

Because of the compression used for the indirect light we are limited to diffuse BRDFs. However, this limitation can be ignored to enable non-diffuse materials by accepting a result that is physically not completely correct.

In Figure 19 different non-diffuse BRDFs are used to show that the augmentations are still plausible. The glossy DRAGON on the left has a Blinn-Phong material [47]. The OTTO bust on the right is shaded with a modified version of our Blinn-Phong material using a rescaled Schlick approximation of the Fresnel term [48] and the BUNNY in the center is rendered with an image space effect to convey the impression of glass. We explain each of these approximations in the following.

Glossy and metallic materials To be able to support different shading models, a few modifications to the rendering pipeline are required and the G-Buffer needs to store additional properties. The VALs are still used for direct rendering but this time the reflectance can change per object or, more precisely, per texel of the G-Buffer. The diffuse indirect lighting, computed by PRT, is still available and can be used by the different materials if desired. In contrast to pure diffuse materials where the irradiance from each VAL can be computed analytically and the amount of reflected light is defined by the constant reflection coefficient ρ, the reflection on glossy materials is view-dependent and thereby more complex. For a correct solution one needs to integrate over the area light source and accumulate the reflected radiance because the BRDF is not constant anymore. To meet the real-time performance requirements, we only use the center of the VAL as a representative sample. For the glossy BRDF we used this approximation and applied the diffuse lighting by PRT leading to a multi-layered material.

For glossy and metallic materials, we added another G-Buffer layer to store specular reflection coefficients and a roughness value. The rescaled Schlick reflection model involves reflection indices with real and imaginary parts instead of diffuse and specular coefficients so we use these slots to store reflection indices for the three color channels. Since the indices are not necessarily in the interval $[0,1]$, the texture format of these two G-Buffer layers is changed to $R16G16B16A16$. During the G-Buffer generation we make use of Dynamic Shader Linkage where each material is represented by a class that fills the buffer with properties required by that material. The free alpha channel of the diffuse layer is used to store an ID to identify the material per texel. During the illumination step of the deferred lighting the same classes are used to evaluate a BRDF function based on the stored ID. This approach allows to apply various different BRDFs as long as the parameters fit into the G-Buffer and the objects are fully opaque.

Note that due to the missing high-resolution environment images on the tablet, we cannot display highly glossy virtual objects. Instead of reflections of all parts of the real environment, only the highlights of the extracted VALs are visible. Since metallic materials reflect all incoming light at the surface, there is no diffuse reflection which technically is a coarse approximation of subsurface scattering. Hence, we do not apply diffuse illumination by PRT in this case, which is the reason for the darker backsides of the busts. As noticeable on the left of the dragons in Figure 19, the indirect illumination for glossy materials is still only diffuse and thereby not plausible for glossy objects.

Translucent materials Non-opaque objects are more complex because another layer is required to allow translucent objects in front of opaque virtual or real surfaces. For the glass shader, the G-Buffer is extended by two depth layers, one for front and one for back faces to estimate the thickness of the glass object. It is also required to introduce another normal buffer to calculate direct illumination, reflection and refraction on the glass surface. The free alpha channel is used to store a flag that indicates whether there is a translucent object at that certain texel or not. If the flag is set during the illumination step, we calculate the direct lighting for the second layer, too and write the accumulated radiance into another output buffer. Note that the opaque objects are processed as before without any influence of this second layer.

Finally, a Post-effect is applied to the augmented image already containing opaque virtual objects. For this effect we evaluate the reflection and refraction ray for each texel with the translucency flag set. Instead of using a more correct ray marching approach we simply project both rays into the augmented image space and use them as offsets to sample corresponding color values. This coarse approximation results in reasonable reflections and refractions if the sampling distance is adjusted properly and the relevant areas are visible in the image. The thickness of the translucent objects is used to estimate a transmittance T based on the Beer-Lambert law. Eq. 16 shows the final composition for marked texels where f is the approximated Fresnel term:

$$L = \max(f\,L_{reflected}, L_{direct}) + (1-f)\;T\;L_{refracted}\;. \tag{16}$$

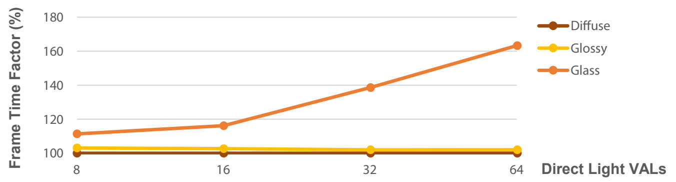

Fig. 20. Rendering overhead on the client for augmenting the CORNELL SCENE with a glossy or a glass BUNNY compared to the former diffuse BRDF, respectively. The overhead factor was measured for different numbers of VALs for direct lighting.

We use the maximum function to get reflections of all frequencies from the image space approach and highlights introduced by sources not directly visible in the image by calculation from VALs. Note that highlights generated by image space reflections are probably too dark because the live camera stream is not an HDR stream and visible light sources are clamped because of saturated texels. Additionally, the shadows of our translucent objects are incorrect, because caustics, which are the result of a correct transmission of light through glass, are also not part of the approximation and thereby a topic of further investigation. Overall, this treatment of glass objects is far away from a physically correct solution but it shows how our approach can be extended to meet the requirements of applications with higher visual complexity.

These changes also have an impact on the performance of the rendering client. The shader classes and the changed G-Buffer layer formats introduced for glossy and metallic BRDFs result in a constant overhead of about $2-3\,\%$ compared to the diffuse material. For rendering glass objects, the additional direct lighting and the Post-effect are leading to an overhead that increases with the number of VALs (see Figure 20).

6.7 Discussion of Parameters

Direct and Indirect Light In Sec. 4.2 we introduced a user parameter τ to control the threshold for splitting direct from indirect light. Figure 21 shows the influence of the parameter selection on the visual quality of the result using different numbers of VALs. The parameter τ defines the percentage of the overall measured radiance, the direct light accounts to. This implies that a low percentage leads to smaller area lights that concentrate in bright regions while large percentages result in larger areas to be sampled (visualized in the first row). Thereby, higher percentages allow other bright areas to be treated as direct, shadow casting light sources. At the same time, increasing τ also leads to decreasing intensity because the area grows while the uniformly distributed average radiance is declining since only darker texels are added to clusters. For very large τ, like in the rightmost column, this leads to wide VALs with relatively low intensity. The effect is even stronger when using a low number of VALs, which results is an ambient like shading. Note that these results differ from the approach of clustered VPLs discussed in Sec. 6.2. Here, point lights with area independent intensities are used, where singularities occur when shading surfaces close to the light position. While selecting a very high τ causes problems, a very low percentage can enhance the visual quality when using a low number of VALs in a scenario with one or two small bright light sources. In this case, the VALs have a small area and are placed close to each other leading to soft shadows (see columns on the left). With increasing τ the light sources drift apart casting shadows from different directions (see columns on the right). In general, one requires more VALs to achieve soft shadows for higher direct light percentages. In our examples, we used $75-98\,\%$ of the total radiant intensity for the direct light.

Resolution of the Atlas In our experiments the atlas resolution was 1024×1024 in the $R32G32B32A32$ format which roughly matches the resolution of the environment cameras. If a camera is very close to the real surface it is possible that valuable information gets lost because of a lower atlas resolution that covers that surface. We consider this an unlikely situation, because in real world applications the cameras will be placed at a certain distance from regions of interest to not distract the users. Furthermore, in digital content creation it is very common to allocate more space for such interesting regions during the atlas parametrization which overcomes this concern if the positions of the environment cameras are known. However, if it is required to increase the atlas resolution the performance impact is restricted to the server.

Resolution of the Cube Maps for indirect Light It is not required to use high resolution cube maps for estimating the indirect light for virtual objects because the SH-projection does not preserve details. If there are fine bright details with visible impact that are smaller than one cube map texel it is very likely that those details should be treated as direct light instead. However, if there are small important details that are not bright enough to be considered direct radiance, these surfaces have to be very close to the virtual object. In this case the surface will be represented in a larger area of the cube map and thereby handled with little errors. We used a $32\times32\times6$ $R32G32B32A32$ cube map for our experiments. We do not recommend lower resolutions since the results can start flickering when moving or rotating the objects. Using higher resolutions showed no improvements.

7 Conclusions and Future Work

We demonstrated that augmented reality with consistent illumination is possible on current mobile devices at interactive frame rates. To achieve this, we developed a lighting method that shares the computation effort among a stationary PC and the participating mobile device. The amount of data to be exchanged between both is reduced, avoiding a bottleneck in transmission due to limited bandwidth. Multiple mobile devices are supported without additional overhead in terms of lighting calculation and transmission since the parameters of the light model are valid for all devices and can be broadcasted. We captured the near-field illumination of indoor scenarios with multiple HDR video cameras and use this as information for the illumination of the virtual objects. The virtual objects can be moved freely with a consistent illumination at any position and adapt to temporal changes in the incident illumination, although the sources of light are not visible to the tablet camera. Although our system is designed for diffuse virtual objects, we also introduced a first approximation for a plausible display of glossy materials.

At present, we place the HDR cameras manually such that all relevant regions are visible in at least one of the cameras. However, if there are regions not visible to any camera, some of the illumination might be missing. To overcome this problem, we want to evaluate a dynamic, tracked HDR camera that can be moved to such invisible regions in the future. This additional information also improves the quality of the captured light sources, since a few static cameras are not enough to capture a goniometric

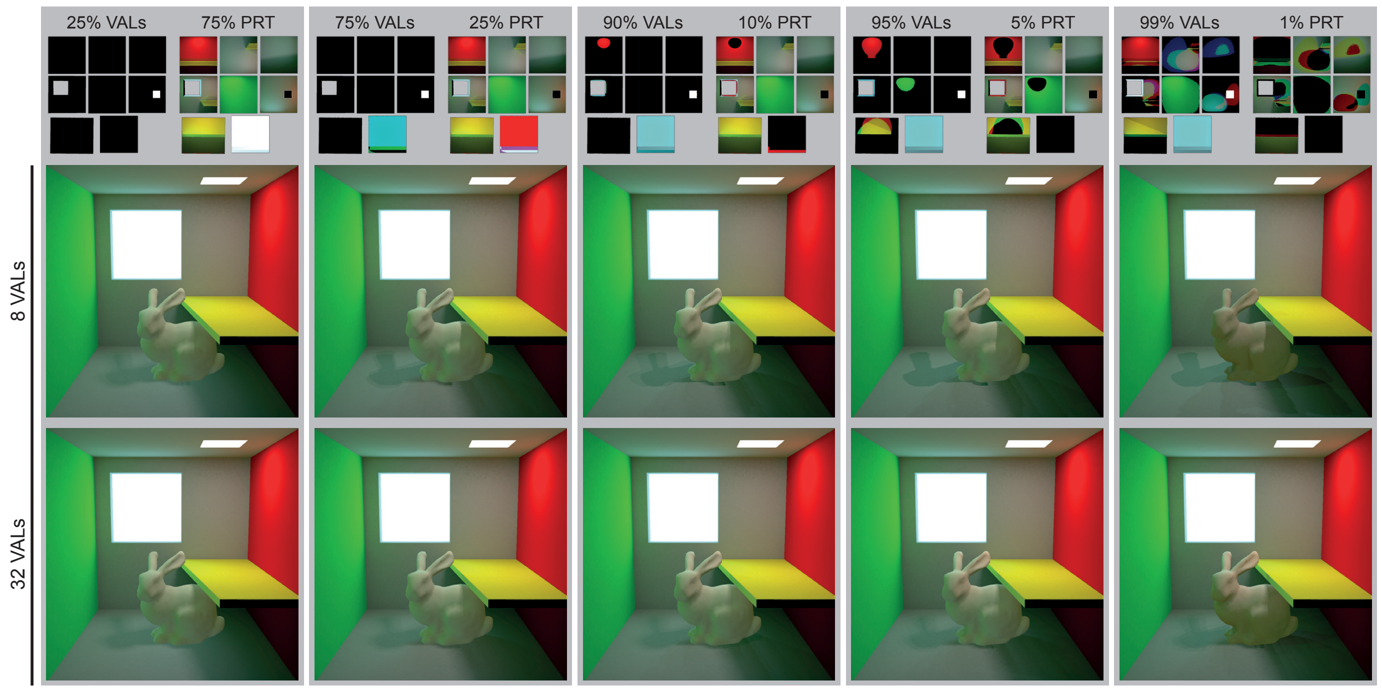

Fig. 21. Comparison of different percentages τ to split direct from indirect light and the impact on the final result using different numbers of VALs.

diagram of a complex light source. The same applies to the capture process of real objects with non-diffuse materials. Since portable 3D sensors are available, dynamic capturing of the geometry and materials is also interesting [33]. Currently, we do not include the indirect illumination which is reflected from the virtual object to the real scene. This could be added by analyzing the radiance distribution on the virtual object and the placement of virtual light sources onto the virtual object. To improve the shadow quality, a soft shadow could be displayed for each area light, similar to [43].

Our method supports manipulation of virtual objects with correct illumination at interactive rates, but the update rates of the direct light sources are lower since they are only updated after a *complete* iteration of the server pipeline (as visible in the accompanying video). Additionally, we neither predict the VAL positions on the client side nor blend between updated and former VALs, which would both hide this latency.

Note that our hardware setup allows for working in a dynamic environment with moving real objects and under changing light conditions. For static environments one could use *only* the mobile devices to capture the surroundings in a preprocess and track visual features for estimating the device position. The presented approach works in this setting without the complex hardware setup, too.

Acknowledgments

This work was sponsored by grant no. GR 3833/2-1 and DA 1319/2-1 of the German Research Foundation (DFG).

References

[1] G. W. Fitzmaurice, S. Zhai, and M. H. Chignell, "Virtual reality for palmtop computers," *ACM Transactions on Information Systems*, vol. 11, no. 3, pp. 197–218, 1993.

[2] A. Fournier, A. Gunavan, and C. Romanzin, "Common illumination between real and computer generated scenes," in *Proc. Graphics Interface (GI)*, 1993, pp. 254–262.

[3] G. Drettakis, L. Robert, and S. Bougnoux, "Interactive common illumination for computer augmented reality," in *Rendering Techniques*, 1997, pp. 45–56.

[4] C. Loscos, M. Frasson, G. Drettakis, B. Walter, X. Granier, and P. Poulin, "Interactive virtual relighting and remodeling of real scenes," in *Proc. EGWR*, 1999, pp. 329–340.

[5] P. Debevec, "Rendering synthetic objects into real scenes: Bridging traditional and image-based graphics with global illumination and high dynamic range photography," in *Proc. SIGGRAPH '98*, 1998, pp. 189–198.

[6] I. Sato, Y. Sato, and K. Ikeuchi, "Acquiring a radiance distribution to superimpose virtual objects onto a real scene," *IEEE Transactions on Visualization and Computer Graphics*, vol. 5, no. 1, pp. 1–12, 1999.

[7] T. Grosch, "Differential photon mapping: Consistent augmentation of photographs with correction of all light paths," in *Eurographics Short Papers*, 2005, pp. 53–56.

[8] M. Corsini, M. Callieri, and P. Cignoni, "Stereo light probe," *Computer Graphics Forum*, vol. 27, no. 2, pp. 291–300, 2008.

[9] J. Unger, S. Gustavson, P. Larsson, and A. Ynnerman, "Free form incident light fields," *Computer Graphics Forum*, vol. 27, no. 4, pp. 1293–1301, 2008.

[10] K. Karsch, V. Hedau, D. Forsyth, and D. Hoiem, "Rendering synthetic objects into legacy photographs," *ACM Transactions on Graphics (Proc. SIGGRAPH Asia)*, vol. 30, no. 6, pp. 157:1–157:12, 2011.

[11] K. Jacobs and C. Loscos, "Classification of illumination methods for mixed reality," *Computer Graphics Forum*, vol. 25, no. 1, pp. 29–51, 2006.

[12] M. Kanbara and N. Yokoya, "Geometric and photometric registration for real-time augmented reality," in *Proc. ISMAR*, 2002, pp. 279–280.

[13] K. Agusanto, L. Li, Z. Chuangui, and N. W. Sing, "Photorealistic rendering for augmented reality using environment illumination," in *Proc. ISMAR*, 2003, pp. 208–216.

[14] M. Haller, S. Drab, and W. Hartmann, "A real-time shadow approach for an augmented reality application using shadow volumes," in *Proc. VRST*, 2003, pp. 56–65.

[15] S. A. Pessoa, G. de S. Moura, J. P. S. M. Lima, V. Teichrieb, and J. Kelner, "Photorealistic rendering for augmented reality: A global illumination and BRDF solution," in *Proc. Virtual Reality (VR)*, 2010, pp. 3–10.

[16] S. Gibson and A. Murta, "Interactive rendering with real-world illumination," in *Proc. EGWR*, 2000, pp. 365–376.

[17] S. Gibson, J. Cook, T. Howard, and R. Hubbold, "Rapid shadow generation in real-world lighting environments," in *Proc. EGSR*, 2003, pp. 219–229.

[18] T. Grosch, "PanoAR: Interactive augmentation of omni-directional images with consistent lighting," in *Mirage, Computer Vision / Computer Graphics Collaboration Techniques and Applications*, 2005, pp. 25–34.

[19] V. Havran, M. Smyk, G. Krawczyk, K. Myszkowski, and H.-P. Seidel, "Importance sampling for video environment maps," in *ACM SIGGRAPH 2005 Sketches*, 2005.

[20] M. Korn, M. Stange, A. von Arb, L. Blum, M. Kreil, K. Kunze, J. Anhenn, T. Wallrath, and T. Grosch, "Interactive augmentation of live images using a HDR stereo camera," in *GI VR/AR*, 2006, pp. 107–118.

[21] T. Grosch, T. Eble, and S. Mueller, "Consistent interactive augmentation of live camera images with correct near-field illumination," in *Proc. VRST*, 2007, pp. 125–132.

[22] M. Knecht, C. Traxler, O. Mattausch, W. Purgathofer, and M. Wimmer, "Differential instant radiosity for mixed reality," in *Proc. ISMAR*, 2010, pp. 99–107.

[23] M. Knecht, C. Traxler, O. Mattausch, and M. Wimmer, "Reciprocal shading for mixed reality," *Computers & Graphics*, vol. 36, no. 7, pp. 846–856, 2012.

[24] P. Kán and H. Kaufmann, "Differential progressive path tracing for high-quality previsualization and relighting in augmented reality," in *Advances in Visual Computing*, G. Bebis, Ed. Springer-Verlag Berlin Heidelberg, 2013, pp. 328–338.

[25] T. A. Franke, "Delta light propagation volumes for mixed reality," in *Proc. ISMAR*, 2013, pp. 125–132.

[26] P. Kán and H. Kaufmann, "High-quality reflections, refractions, and caustics in augmented reality and their contribution to visual coherence," in *Proc. ISMAR*, 2012, pp. 99–108.

[27] D. Nowrouzezahrai, S. Geiger, K. Mitchell, R. Sumner, W. Jarosz, and M. Gross, "Light factorization for mixed-frequency shadows in augmented reality," in *Proc. ISMAR*, 2011, pp. 173–179.

[28] M. Aittala, "Inverse lighting and photorealistic rendering for augmented reality," *The Visual Computer*, vol. 26, no. 6-8, pp. 669–678, 2010.

[29] D. A. Calian, K. Mitchell, D. Nowrouzezahrai, and J. Kautz, "The shading probe: Fast appearance acquisition for mobile AR," in *SIGGRAPH Asia Technical Briefs*, 2013, pp. 20:1–20:4.

[30] Y. Yao, H. Kawamura, and A. Kojima, "The hand as a shading probe," in *ACM SIGGRAPH Posters*, 2013, pp. 108:1–108:1.

[31] C. B. Madsen and B. B. Lal, "Outdoor illumination estimation in image sequences for augmented reality," in *Proc. GRAPP*, 2011, pp. 129–139.

[32] J. Jachnik, R. A. Newcombe, and A. J. Davison, "Real-time surface light-field capture for augmentation of planar specular surfaces," in *Proc. ISMAR*, 2012, pp. 91–97.

[33] P. Lensing and W. Broll, "Instant indirect illumination for dynamic mixed reality scenes," in *Proc. ISMAR*, 2012, pp. 109–118.

[34] M. Meilland, C. Barat, and A. Comport, "3D High Dynamic Range Dense Visual SLAM and Its Application to Real-time Object Re-lighting," in *Proc. ISMAR*, 2013, pp. 143–152.

[35] L. Gruber, T. Richter-Trummer, and D. Schmalstieg, "Real-time photometric registration from arbitrary geometry," in *Proc. ISMAR*, 2012, pp. 119–128.

[36] L. Gruber, T. Langlotz, P. Sen, T. Hoellerer, and D. Schmalstieg, "Efficient and robust radiance transfer for probeless photorealistic augmented reality," in *Proc. Virtual Reality (VR)*, 2014, pp. 91–97.

[37] M. Csongei, L. Hoang, C. Sandor, and Y. B. Lee, "Global illumination for augmented reality on mobile phones (Poster)," in *Proc. Virtual Reality (VR)*, 2014, pp. 69–70.

[38] E. H. Adelson and J. R. Bergen, "The plenoptic function and the elements of early vision," in *Computational Models of Visual Processing*, 1991, vol. 1, no. 2, pp. 3–20.

[39] T. Ritschel, C. Dachsbacher, T. Grosch, and J. Kautz, "The state of the art in interactive global illumination," *Computer Graphics Forum*, vol. 31, no. 1, pp. 160–188, 2012.

[40] A. Keller, "Instant Radiosity," in *Proc. SIGGRAPH '97*, 1997, pp. 49–56.

[41] P.-P. J. Sloan, J. Kautz, and J. Snyder, "Precomputed radiance transfer for real-time rendering in dynamic, low-frequency lighting environments," *ACM Transactions on Graphics (Proc. SIGGRAPH)*, vol. 21, no. 3, pp. 527–536, 2002.

[42] J. T. Kajiya, "The rendering equation," *Computer Graphics (Proc. SIGGRAPH)*, vol. 20, no. 4, pp. 143–150, 1986.

[43] Z. Dong, T. Grosch, T. Ritschel, J. Kautz, and H.-P. Seidel, "Real-time indirect illumination with clustered visibility," in *Vision, Modeling, and Visualization Workshop*, 2009, pp. 187–196.

[44] R. Ramamoorthi and P. Hanrahan, "An efficient representation for irradiance environment maps," in *Proc. SIGGRAPH '01*, 2001, pp. 497–500.

[45] J. Andersson, "Parallel Graphics in Frostbite - current & future," *SIGGRAPH Course: Beyond Programmable Shading*, 2009.

[46] G. Greger, P. Shirley, P. M. Hubbard, and D. P. Greenberg, "The irradiance volume," *IEEE Computer Graphics and Applications*, vol. 18, no. 2, pp. 32–43, 1998.

[47] N. Hoffman, "Physically based shading models for film and game production," in *SIGGRAPH Course*, 2010.

[48] I. Lazányi and L. Szirmay-Kalos, "Fresnel term approximations for metals," in *WSCG (Short Papers)*, 2005, pp. 77–80.

Kai Rohmer works as a scientific researcher in the Computational Visualistics Group at the Department of Simulation and Graphics at the University of Magdeburg, Germany. His research interests include physically-based real-time rendering as well as augmented reality on mobile devices. He received his MSc in computer science with distinction in 2012.

Wolfgang Büschel received his MSc in computational visualistics with distinction in 2012 and is currently working toward the PhD degree at the Interactive Media Lab at Technische Universität Dresden, Germany. His research interests include natural user interfaces and advanced interaction techniques for augmented reality.

Raimund Dachselt is university professor at the Technische Universität Dresden, Germany, where he heads the Interactive Media Lab Dresden. His background and research interest are 3D user interfaces, natural human-computer interaction and information visualization. He has published extensively, served in numerous programming committees, and co-organized several international conferences and workshops. Dr. Dachselt is a member of the IEEE and the IEEE Computer Society, ACM SIGCHI and SIGMM.

Thorsten Grosch is a junior professor at the University of Magdeburg, Germany, where he heads the Computational Visualistics Group at the Department of Simulation and Graphics. His research interests include both physically-based and real-time global illumination methods for virtual and augmented reality.